nanoenergy advances

MDPI

Article

Modeling Particle-Doped Materials for Performance Improvement of Contact-Separation Triboelectric Nanogenerators

Carlos Callaty *, Isabel Gonçalves, Cátia Rodrigues and João Ventura *

IFIMUP (Institute of Physics for Advanced Materials, Nanotechnology and Photonics), Department of Physics and Astronomy, Faculty of Sciences, University of Porto, Rua do Campo Alegre, s/n, 4169-007 Porto, Portugal
* Correspondence: up201304115@edu.fc.up.pt (C.C.); joventur@fc.up.pt (J.V.)

Abstract: Triboelectric nanogenerators (TENGs) are an attractive energy harvesting technology due to their high efficiency and vast applications in self-powered sensors. In this work, dielectric–dielectric contact-separation TENGs were modeled with time-dependent finite element simulations with the objective of improving TENG's performance by enhancing the relative permittivity (ε_r).To achieve this, the chosen material (PDMS, $\varepsilon_r = 2.75$) was doped with $SrTiO_3$ (ε_r = 300) particles. The open-circuit voltage (V_{OC}) and short-circuit current (I_{SC}) remained constant as ϵ_r increased, as predicted by existent models, but in contradiction with available experimental data. Thus, we introduced a charge correction model relating ϵ_r and surface charge density, allowing us to observe an increase in TENG performance output (V_{OC} and I_{SC}). This work shows that finite element simulations are suitable for better understanding and optimizing TENGs' performance.

Keywords: triboelectric nanogenerator; numerical simulations; particle-doped PDMS; relative permittivity

check for updates

Citation: Callaty, C.; Gonçalves, I.; Rodrigues, C.; Ventura, J. Modeling Particle-Doped Materials for Performance Improvement of Contact-Separation Triboelectric Nanogenerators. *Nanoenergy Adv.* **2024**, *4*, 147–155. https://doi.org/10.3390/nanoenergyadv4020009

Academic Editor: Ya Yang

Received: 11 December 2023
Revised: 22 March 2024
Accepted: 12 April 2024
Published: 30 April 2024

1. Introduction

A triboelectric nanogenerator (TENG) is an energy harvester device that converts mechanical into electrical energy [1,2], while being environmentally friendly [3,4], making it an interesting energy source to help mitigate the present climate crisis [5–7]. TENGs have a vast potential for self-power sensor applications [3,8–11], powering self-sustainable devices (such as floating buoys [3,12–14] and wearables [3,8,15–18]) and bio-medical [19,20]. From the four TENG operations modes (contact-separation [1,21], sliding [1,22], single-electrode [1,23] and freestanding layer [1]), research focuses on enhancing output power (P) [24] and on modeling the working mechanisms [1,21,25–27] and contact properties [11,28]. One of the most important paths to enhance P is by improving material parameters such as relative permittivity (ε_r) and surface charge density (σ) [29,30]. One way to improve ε_r is by doping the triboelectric layers such as PDMS (Polydimethylsiloxane) [29,31–33], PMMA (Poly(methyl 2-methylpropenoate)) [34] and BMF (bamboo microfibrils) [35] with high ε_r particles, such as $BaTiO_3$ [29,31–33], $CaCu_3Ti_4O_{12}$ [35] and $SrTiO_3$ [29]. The effective relative permittivity (ε_{eff}) of materials doped with particles will then be given by [29]:

$$\varepsilon_{eff} = \varepsilon_{r_1} f_1 + \varepsilon_{r_2} f_2, \tag{1}$$

where ε_{r_1} and ε_{r_2} are the relative permittivities of the matrix and particles, and f_1 and f_2 are the corresponding concentration fractions.

In particular, PDMS is attracting attention for its mature, low-cost manufacturing and flexibility [19,36]. References [29,32] showed that it is possible to combine PDMS with particle doping to improve TENG performances. However, having very high concentrations ($\gtrsim$10%) of particles leads to a decrease in surface contact area, decreasing TENG's performance [29]. Therefore, one has to search for the optimal particle concentration [29,32,35]

at the expense of a large amount of time and resources. To prevent this, the best option is to numerically model TENG materials with varying particle concentrations as a guide to obtaining optimal values experimentally. In fact, recent developments in finite element simulations have opened up new possibilities to simulate TENG performance and guide its optimization [11,37–40]. Numerical simulations are key not only to validating but also to predicting novel results when developing experimental setups or materials, decreasing the time spent in optimization. Performing time-dependent numerical simulations conjugating the relative motion of two materials and the resulting electrostatic spatial distribution has been a challenge for TENGs that has only recently been surpassed [37].

Research on TENGs using COMSOL has been performed recently for, e.g., heat TENG self-sustained sensors [11] and hybrid TENG and thermoelectric nanogenerators [40]. However, a detailed study on how to perform and optimize COMSOL TENG simulations has not yet been performed. Research on stationary simulations, where the device is simulated in one instant of time, was conducted by Hasan et al. [38]. However, time-dependent simulations allow for more realistic analysis, such as the charge transference processes occurring in TENGs. In that regard, Chen et al. [37] performed simulations on COMSOL Multiphysics with time-dependent simulations using contact-separation and sliding TENGs modes by using the moving mesh.

Niu et al. [21] modeled the contact-separation TENG as a double parallel-plate capacitor, with two electrodes, two dielectrics (for the dielectric–dielectric mode), and a varying air gap. By calculating the electric field in the dielectric and air gap, the voltage (V) is obtained:

$$V = -\frac{Q}{S\varepsilon_0}\left(\frac{d_1}{\varepsilon_{r_1}} + \frac{d_2}{\varepsilon_{r_2}} + x(t)\right) + \frac{\sigma x(t)}{\varepsilon_0}, \tag{2}$$

where Q is the charge in the electrodes, S the TENG's area, σ the surface charge density of both dielectrics, d_1 and d_2 are the thicknesses of both dielectrics and ε_{r_1}, ε_{r_2} the corresponding relative permittivities and $x(t)$ the time-dependent distance between the dielectrics.

Adding a load resistance (R_L) to simulate the delivery of the harvested energy to an external circuit, two special cases arise. At low resistances, V is negligible and Equation (2) gives the short-circuit current (I_{SC}):

$$I_{SC} = \frac{S\sigma v(t) d_0}{(d_0 + x(t))^2}, \tag{3}$$

where $v(t)$ is the velocity of the moving layer of the TENG and $d_0 = \frac{d_1}{\varepsilon_{r_1}} + \frac{d_2}{\varepsilon_{r_2}}$. At high resistances (open-circuit region), the charge in the electrodes is negligible, allowing the determination of the open-circuit voltage (V_{OC}):

$$V_{OC} = \frac{\sigma x(t)}{\varepsilon_0}. \tag{4}$$

In this work, we simulated contact-separation TENGs with particle-doped materials for better optimization of the concentration, maximizing TENG's performance. Furthermore, a comparison between particle and ε_{eff} models is provided.

2. Numerical Procedures

Based on Niu's model [21], a dielectric–dielectric contact-separation TENG was simulated using COMSOL Multiphysics. To reduce the complexity of the model, the simulations were performed in 2D, with an out-of-plane thickness of 1 mm, due to COMSOL always performing simulations in 3D. The accuracy and optimization of the numerical simulations were based on our previous work [27]. The TENG was built in the *Geometry* node and inserted inside a box of air large enough not to interfere with the results (Figure 1a). Nylon and PMDS were the chosen dielectric materials and copper was chosen for the electrodes. The top electrode/Nylon pair has a uniform movement with respect to the

bottom electrode/particle-doped PDMS, which is kept at rest. To simulate particles, 15 µm circles (with ε_r = 300 [29] corresponding to $SrTiO_3$) were distributed uniformly inside the PDMS using the *Geometry* node. The 15 µm value was chosen after time and convergence optimization while allowing us to cover a significant concentration and relative permittivity range. The use of smaller particles (in the nanosize range) would lead to far more complex and time-demanding simulations, also affecting convergence. Finally, a mesh with triangular shapes was created with the maximum size defined with the "finner" size in COMSOL, which was the best option to reduce simulation time without affecting the final results.

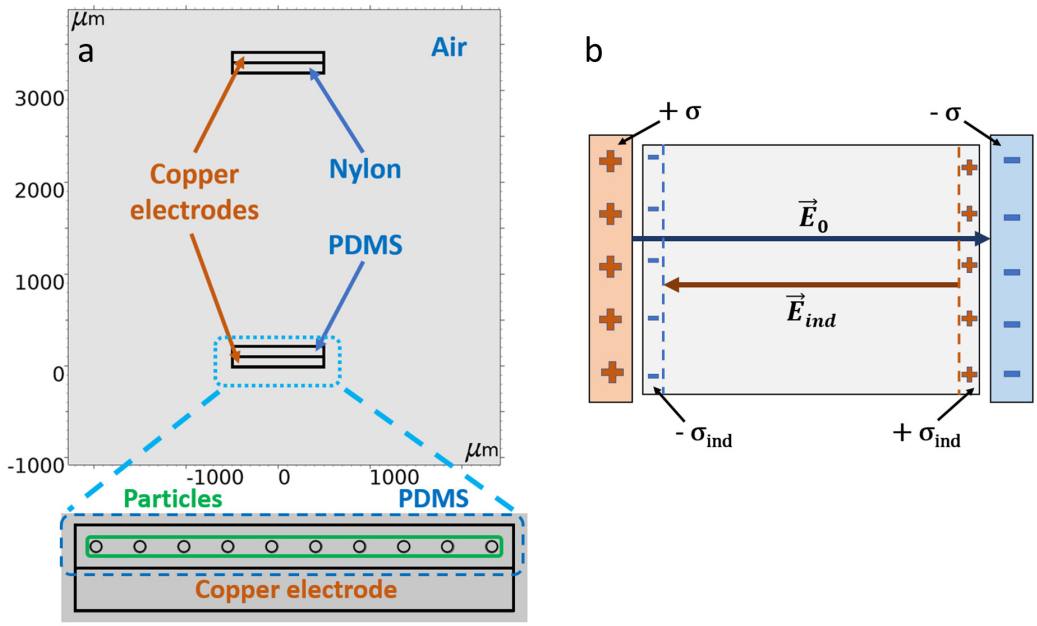

Figure 1. (**a**) Contact-separation TENG represented in COMSOL and corresponding zoom in the PDMS/bottom electrode where the $SrTiO_3$ particles can be observed. The displayed $SrTiO_3$ particle concentration on PDMS is 7.1%. (**b**) Two electrodes with opposing total σ and the dielectric medium where, at the borders with the electrodes, a charge equilibrium is reached.

A comparison between PDMS with particles and PDMS with an equivalent ε_{eff} was performed to evaluate the effect of ε_{eff} for constant σ. Since researchers performing experiments with doped-nanoparticle TENG materials have observed an increase in the generated V_{OC} and I_{SC} with particle concentration [29,34,41] and ε_r (until an optimal value is reached), one must consider a relation between ε_{eff} and σ. This relationship is still not well understood, and there is no model that accurately describes it. Inspired by the trends observed in Ref. [34], we related ε_r and σ by modeling the contact-separation TENG as a parallel-plate capacitor with a dielectric medium (Figure 1b) with a ε_{eff}, for which the total electrical field is given by

$$E_{total} = E_0 - E_{ind}, \tag{5}$$

with E_0 the electric field in vacuum and E_{ind} the induced electric field of PDMS. The electric fields can be written as:

$$\frac{\sigma}{\varepsilon_0 \varepsilon_{eff}} = \frac{\sigma}{\varepsilon_0} - \frac{\sigma_{ind}}{\varepsilon_0}, \tag{6}$$

where σ is the total surface charge density and σ_{ind} the surface charge density induced on the materials. This can be rearranged as:

$$\sigma_{ind} = \sigma\left(\frac{\varepsilon_{eff} - 1}{\varepsilon_{eff}}\right). \tag{7}$$

To simulate the PDMS reference case, we used $\sigma_{ref} = 6 \times 10^{-4}$ cm^{-2} as σ_{ind} and obtained the total surface charge density value (9.42×10^{-4} cm^{-2}). With these values, simulations were performed comparing particle-doped PDMS and a PDMS with an equivalent ε_{eff} with σ varying in both cases according to Equation (7).

To evaluate TENG's performance, R_L ranging from 1 MΩ to 1.2 GΩ were used allowing us to obtain the maximum power output (P_{max}), while 100 Ω and 100 TΩ were used to obtain I_{SC} and V_{OC}, respectively. The values used for the simulations are listed in Table 1. The $SrTiO_3$ particle-doped concentration and ε_{eff} values simulated are listed in Table 2. The ε_{eff} values were obtained from Equation (1) by considering $SrTiO_3$ with ε_r and particle concentration fractions (f) listed in Table 2 and PDMS ε_r and fraction $(1 - f)$.

Table 1. List of parameters and corresponding base values. The out-of-plane thickness is the same as the width of the nylon/PDMS/copper electrode, giving a TENG area of 1×10^{-6} m^2. σ values were based on Chen et al. [29] experimental values (in the range 10^{-5}–10^{-4} C/m^2).

Parameter	Value
Velocity	5.999 m/s
Period	1×10^{-3} s
Number of periods (cycles)	3
Time per step	1×10^{-6} s
σ of nylon	6×10^{-4} C/m^2
σ of PDMS	-6×10^{-4} C/m^2
ε_r of nylon	4
ε_r of PDMS	2.75
Width/Height of the air box	0.1 m
Height/thickness of nylon/PDMS/electrodes of cooper	1×10^{-4} m
Width of PDMS/nylon/electrodes of cooper	1×10^{-3} m
Maximum distance between nylon and PDMS surfaces	3×10^{-3} m
Minimum distance between planes	2.1×10^{-5} m

Table 2. List of $SrTiO_3$ particle concentrations and ε_{eff} values.

Concentration	ε_{eff}
0.7%	4.9
1.4%	7.0
2.8%	11.1
4.2%	15.4
5.7%	19.6
7.1%	23.8
8.5%	28.0

3. Numerical Results

In this section, PDMS doped with different concentrations will be compared with an equivalent ε_{eff} PDMS with (i) a constant and (ii) a varying surface charge density (according to Equation (7)).

3.1. Constant Surface Charge Density Model

Figure 2 shows the comparison between varying the $SrTiO_3$ particle concentration and varying ε_{eff} for V_{OC} (Figure 2a), I_{SC} (Figure 2b), V (Figure 2c) and current (I) (Figure 2d). Figure 2a,b show a rather constant trend (note the scale), which is the expected outcome according to Niu's model. Also, both I_{SC} and V_{OC} are similar in value for particle concentration and ε_{eff}, meaning both models match. However, in Figure 2c,d, with R_L close to P_{max}, the values of the generated voltage for the particle-doped and equivalent ε_{eff} cases

are significantly different, while the I trends are similar. Regardless, the tendencies for V and I with R_L are within Niu's model's expectation, with I saturating at a maximum value for low R_L, and V increasing with the increase in R_L. Also, the decrease in V and I with the increase in ε_r at constant σ agrees with Niu's model.

An important remark is that in Figure 2a,c, V_{OC} and V have different tendencies due to the V case corresponding to the situation where the electrodes are near the saturation and high R_L contributes to a lower charge flow and does not allow the electrodes to discharge from the saturated state [27]. In this case, and according to Equation (2), if ε_r increases, V decreases. On the other hand, the V_{OC} case (Figure 2a), for which the charge of the electrode is zero (Equation (4)), predicts that V_{OC} is independent of ε_r, therefore remaining constant as ε_{eff} increases.

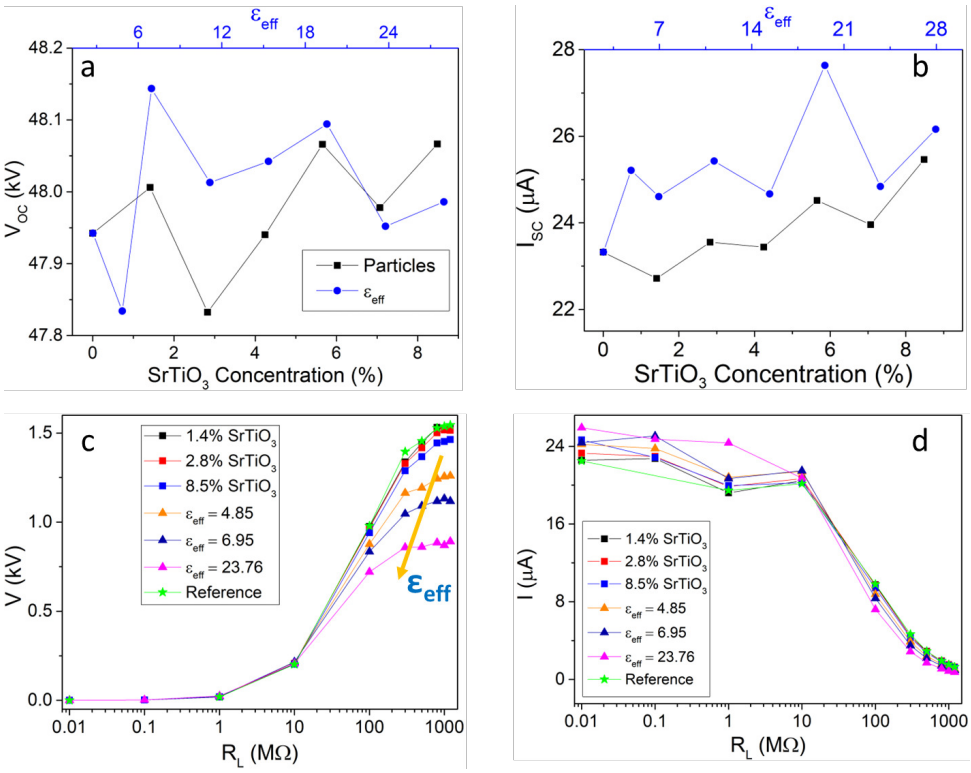

Figure 2. (**a**) V_{OC} and (**b**) I_{SC} as a function of ε_{eff} and $SrTiO_3$ particle concentration on PDMS. (**c**) V and (**d**) I for particle-doped and ε_{eff} PDMS as a function of R_L. The ε_{eff} values were obtained from Equation (1), with the obtained values for each particle concentration being displayed in Table 2.

3.2. Varying Surface Charge Density

To match with the experimentally observed trends, we performed numerical simulations using the ε_r and σ relation of (Equation (7)), resulting in clearly different V_{OC}, I_{SC} and P_{max} behaviors (Figure 3). In this case, V_{OC} and I_{SC} (Figure 3a,c) increase with particle concentration and ε_{eff} in a similar way, agreeing with Niu's model's expected tendencies through the increase in σ with ε_{eff}. On the other hand, although P_{max} also increases with particle concentration and ε_{eff} (Figure 3e), this increase is different for both cases, with the particle concentration case having a higher increase.

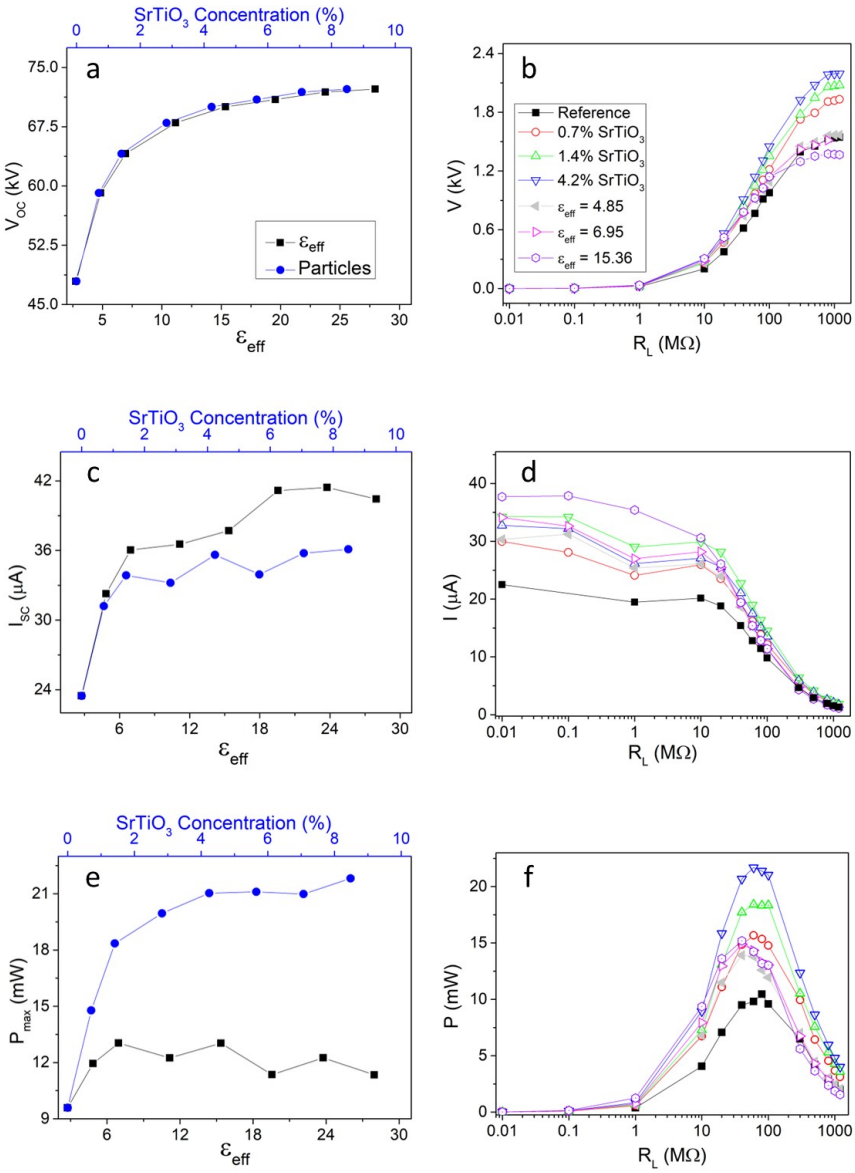

Figure 3. (**a**) V_{OC}, (**c**) I_{SC} and (**e**) P_{max} as a function of ε_{eff} and of $SrTiO_3$ particle concentration on PDMS. (**b**) V, (**d**) I and (**f**) P for particle-doped and ε_{eff} PDMS and as a function of R_L. All figures have σ corrected according to Equation (7).

For R_L near P_{max}, the results show that the $\sigma(\varepsilon_r)$ increase leads to an increase in V, I and P (Figure 3b,d,f) both for increasing particle concentration and ε_{eff}. This is expected from Niu's model's predictions. However, when comparing the particle and ε_{eff} cases, there is a disagreement for V and P's results, agreeing only in the obtained trends.

An important remark from the ε_r and σ relation is that, because COMSOL does not support collisions, at the minimum distance considered (21 µm), both terms of Equation (2) are important because the minimum charge on the electrode (Q) is not negligible and the minimum distance is comparable with the Nylon and PDMS thicknesses (100 µm). This causes a change in the V and P trends at low and high R_L (Figure 4a). At low R_L, the σ term is the dominant one due to the charge in the electrode approaching zero. This leads to an increase in V and P with ε_r. At high R_L, the electrode becomes charge saturated and the charge on the electrode does not decrease much while at the minimum distance (Figure 4b), causing the decrease in V and P with ε_r. At high ε_{eff}, P_{max} is constant (Figure 4a), which agrees with Niu's model (Equation (2)), due to ε_{eff} being much larger

than Nylon's permittivity (4.0), reducing Equation (2) to the metal–dielectric contact-separation TENG case.

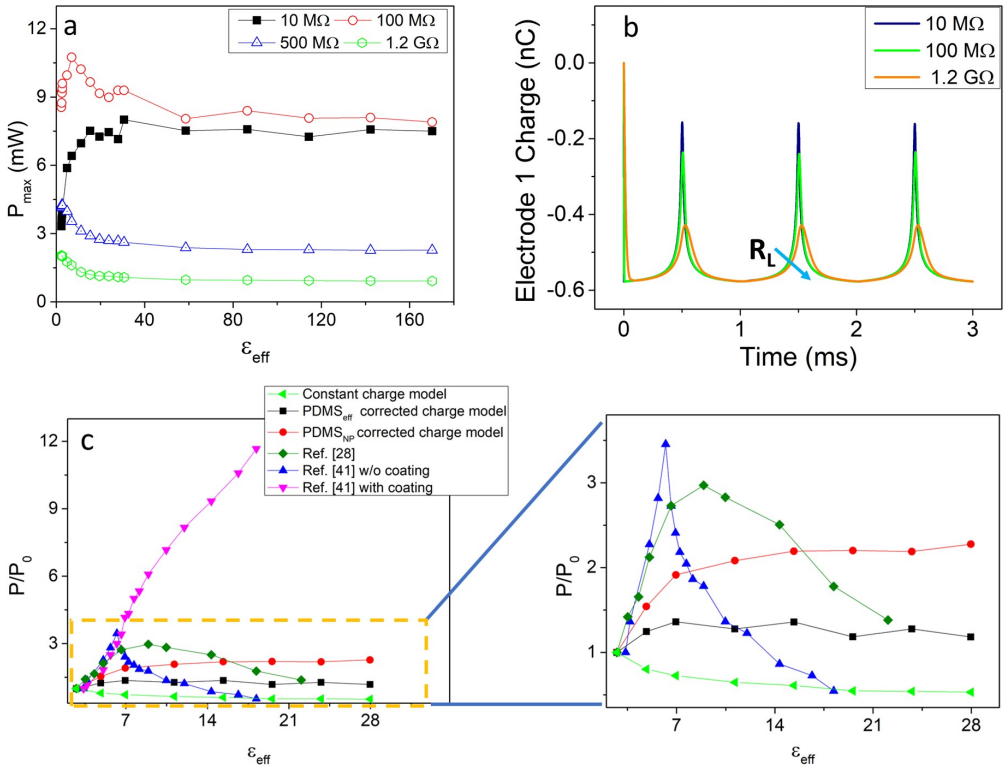

Figure 4. (**a**) P_{max} as a function of ε_{eff}. (**b**) Time variation in the charge in the lower electrode for different R_L values. (**c**) Power output (P) normalized to the power output of the PDMS solely value (P_0) as a function of ε_{eff} of the obtained results compared with available literature.

A final remark about the charge model we developed is that it shows that it is possible to relate ε_r and σ with dynamic finite element numerical simulation. However, despite the final trend being able to predict the available experimental data from literature [29,34,41], the developed model does not take into account additional effects that result in a decrease in σ, such as saturating the surface with nanoparticles [29,41] or current leakage [35]. Figure 4c shows a comparison between the numerical results obtained here and the experimental results obtained by Chen et al. [29] and Zhou et al. [41] normalized to the undoped case. The results from the literature usually show a maximum output at a critical ε_{eff} value, after which there is a decrease in the P/P_0 ratio with ε_{eff}, associated with nanoparticle saturation at the film surface. Ultimately, this may even lead to a decrease in P below that of the undoped sample [41]. A special approach was proposed in Ref. [41] by adding a thin PDMS coating on top of the nanoparticle-doped sample, so that the nanoparticle saturation at the surface does not hinder σ, allowing for it to increase with ε_{eff}.

4. Conclusions

This work enabled the study of TENGs with particle-doped PDMS using time-dependent finite element simulations. The results were compared with those of a material with an equivalent ε_{eff}. While particle-doped and equivalent ε_{eff} PDMS results do not match (except for V_{OC} and I_{SC}), their tendencies are similar and in agreement with those of existent models. For the constant σ simulations, while the tendencies agree with existing models (V_{OC} and the I_{SC} constant, and the decrease in V and I with ε_r), experimental research found that with the increase in ε_r, V_{OC}, I_{SC} and P_{max} increase as well. These tendencies were then observed only with the proposed σ correction and ε_r dependence.

One important remark is that since COMSOL Multiphysics does not support collisions, requiring a minimum distance to be defined, important material properties such as Young's modulus or adhesion strength are not taken into account.

This work thus opens new ways to use time-dependent finite-element simulations for TENGs with complex materials and paves the way to find an improved $\sigma(\varepsilon_r)$ relation for more accurate simulations.

Author Contributions: Conceptualization, C.C., I.G. and C.R.; Investigation, C.C.; writing—original draft preparation, C.C.; writing—review and editing, C.C., I.G., C.R. and J.V.; supervision, J.V. All authors have read and agreed to the published version of the manuscript.

Funding: The authors acknowledge funding from projects 2022.05030.PTDC (https://doi.org/10.54499/2022.05030.PTDC), UIDB/04968/2020 from FCT. This study is supported by the HORIZON-EIC-2022-PATHFINDERCHALLENGES-01project Blood2Power (grant agreement number 101115525) funded by the European Union. FSE/POPH, FEDER, COMPETE and ON2 are also acknowledged. C. Rodrigues is thankful to FCT for grant SFRH/BD/147811/2019.

Data Availability Statement: The data are available upon reasonable request from the corresponding authors.

Conflicts of Interest: This research received no external funding.

References

1. Niu, S.; Wang, Z.L. Theoretical systems of triboelectric nanogenerators. *Nano Energy* **2014**, *14*, 161–192. [CrossRef]
2. Lin, Z.; Chen, J.; Yang, J. Recent Progress in Triboelectric Nanogenerators as a Renewable and Sustainable Power Source. *J. Nanomater.* **2016**, *2016*, 5651613. [CrossRef]
3. Luo, J.; Wang, Z.L. Recent progress of triboelectric nanogenerators: From fundamental theory to practical applications. *EcoMat* **2020**, *2*, e12059. [CrossRef]
4. Wu, C.; Wang, A.C.; Ding, W.; Guo, H.; Wang, Z.L. Triboelectric Nanogenerator: A Foundation of the Energy for the New Era. *Adv. Energy Mater.* **2019**, *9*,1802906. [CrossRef]
5. Liu, Z.; Ciais, P.; Deng, Z.; Lei, R.; Davis, S.; Feng, S.; Zheng, B.; Cui, D.; Dou, X.; Zhu, B.; et al. Near-real-time monitoring of global CO_2 emissions reveals the effects of the COVID-19 pandemic. *Nat. Commun.* **2020**, *11*, 5172. [CrossRef] [PubMed]
6. Technical, I.; Shukla, P.; Skea, J.; Slade, R.; van Diemen, R.; Haughey, E.; Malley, J.; Pathak, M.; Pereira, J.P. *Climate Change and Land: An IPCC Special Report on Climate Change, Desertification, Land Degradation, Sustainable Land Management, Food Security, and Greenhouse Gas Fluxes In Terrestrial Ecosystems*; Intergovernmental Panel on Climate Change: Geneva, Switzerland, 2019; pp. 35–74.
7. Toreti, A.; Bavera, D.; Acosta Navarro, J.; Cammalleri, C.; de Jager, A.; Di Ciollo, C.; Hrast Essenfelder, A.; Maetens, W.; Magni, D.; Masante, D.; et al. *Drought in Europe—August 2022*; Publications Office of the European Union: Luxembourg, 2022; JRC130493, p. 24. [CrossRef]
8. Ma, M.; Kang, Z.; Liao, Q.; Zhang, Q.; Gao, F.; Zhao, X.; Zhang, Z.; Zhang, Y. Development, applications, and future directions of triboelectric nanogenerators. *Nano Res.* **2018**, *11*, 2951–2969. [CrossRef]
9. Askari, H.; Hashemi, E.; Khajepour, A.; Khamesee, M.B.; Wang, Z.L. Towards self-powered sensing using nanogenerators for automotive systems. *Nano Energy* **2018**, *53*, 1003–1019. [CrossRef]
10. Wang, S.; Lin, L.; Wang, Z.L. Triboelectric nanogenerators as self-powered active sensors. *Nano Energy* **2015**, *11*, 436–462. [CrossRef]
11. Xia, K.; Zhu, Z.; Zhang, H.; Xu, Z. A triboelectric nanogenerator as self-powered temperature sensor based on PVDF and PTFE. *Appl. Phys. A Mater. Sci. Process.* **2018**, *124*, 520. [CrossRef]
12. Rodrigues, C.; Nunes, D.; Clemente, D.; Mathias, N.; Correia, J.M.; Rosa-Santos, P.; Taveira-Pinto, F.; Morais, T.; Pereira, A.; Ventura, J. Emerging triboelectric nanogenerators for ocean wave energy harvesting: State of the art and future perspectives. *Energy Environ. Sci.* **2020**, *13*, 2657–2683. [CrossRef]
13. Li, R.; Li, Y.; Zhao, Y.; Li, Y.; Li, Y. Harvest of ocean energy by triboelectric generator technology. *Appl. Phys. Rev.* **2018**, *5*, 031303. [CrossRef]
14. Gonçalves, I.; Rodrigues, C.; Ventura, J. Sea State Adaptation Enhances Power Output of Triboelectric Nanogenerators for Tailored Ocean Wave Energy Harvesting. *Adv. Energy Mater.* **2023**, *14*, 2302627. [CrossRef]
15. Rodrigues, C.; Gomes, A.; Ghosh, A.; Pereira, A.; Ventura, J. Power-generating footwear based on a triboelectric-electromagnetic-piezoelectric hybrid nanogenerator. *Nano Energy* **2019**, *62*, 660–666. [CrossRef]
16. Dassanayaka, D.G.; Alves, T.M.; Wanasekara, N.D.; Dharmasena, I.G.; Ventura, J. Recent Progresses in Wearable Triboelectric Nanogenerators. *Adv. Funct. Mater.* **2022**, *32*, 2205438. [CrossRef]
17. Liu, M.; Pu, X.; Jiang, C.; Liu, T.; Huang, X.; Chen, L.; Du, C.; Sun, J.; Hu, W.; Wang, Z.L. Large-Area All-Textile Pressure Sensors for Monitoring Human Motion and Physiological Signals. *Adv. Mater.* **2017**, *29*, 1–9. [CrossRef] [PubMed]

18. Song, W.; Gan, B.; Jiang, T.; Zhang, Y.; Yu, A.; Yuan, H.; Chen, N.; Sun, C.; Wang, Z.L. Nanopillar Arrayed Triboelectric Nanogenerator as a Self-Powered Sensitive Sensor for a Sleep Monitoring System. *ACS Nano* **2016**, *10*, 8097–8103. [CrossRef] [PubMed]
19. Wang, H.; Cheng, J.; Wang, Z.; Ji, L.; Wang, Z.L. Triboelectric nanogenerators for human-health care. *Sci. Bull.* **2021**, *66*, 490–511. [CrossRef]
20. Zheng, Q.; Shi, B.; Li, Z.; Wang, Z.L. Recent Progress on Piezoelectric and Triboelectric Energy Harvesters in Biomedical Systems. *Adv. Sci.* **2017**, *4*, 1700029. [CrossRef] [PubMed]
21. Niu, S.; Wang, S.; Lin, L.; Liu, Y.; Zhou, Y.S.; Hu, Y.; Wang, Z.L. Theoretical study of contact-mode triboelectric nanogenerators as an effective power source. *Energy Environ. Sci.* **2013**, *6*, 3576–3583. [CrossRef]
22. Niu, S.; Liu, Y.; Wang, S.; Lin, L.; Zhou, Y.S.; Hu, Y.; Wang, Z.L. Theory of Sliding-Mode Triboelectric Nanogenerators. *Adv. Mater.* **2013**, *25*, 6184–6193. [CrossRef]
23. Niu, S.; Liu, Y.; Wang, S.; Lin, L.; Zhou, Y.S.; Hu, Y.; Wang, Z.L. Theoretical investigation and structural optimization of single-electrode triboelectric nanogenerators. *Adv. Funct. Mater.* **2014**, *24*, 3332–3340. [CrossRef]
24. Chen, H.; Xu, Y.; Zhang, J.; Wu, W.; Song, G. Theoretical System of Contact-Mode Triboelectric Nanogenerators for High Energy Conversion Efficiency. *Nanoscale Res. Lett.* **2018**, *13*, 346. [CrossRef] [PubMed]
25. Shao, J.; Jiang, T.; Tang, W.; Chen, X.; Xu, L.; Wang, Z.L. Structural figure-of-merits of triboelectric nanogenerators at powering loads. *Nano Energy* **2018**, *51*, 688–697. [CrossRef]
26. Shao, J.; Willatzen, M.; Wang, Z.L. Theoretical modeling of triboelectric nanogenerators (TENGs). *J. Appl. Phys.* **2020**, *128*, 111101. [CrossRef]
27. Callaty, C.; Gonçalves, I.; Rodrigues, C.; Ventura, J. Modeling the performance of contact-separation triboelectric nanogenerators. *Curr. Appl. Phys.* **2023**, *50*, 100–106. [CrossRef]
28. Hossain, N.A.; Razavi, M.J.; Towfighian, S. Analysis of mechanical deformation effect on the voltage generation of a vertical contact mode triboelectric generator. *J. Micromech. Microeng.* **2020**, *30*, 045009. [CrossRef] [PubMed]
29. Chen, J.; Guo, H.; He, X.; Liu, G.; Xi, Y.; Shi, H.; Hu, C. Enhancing Performance of Triboelectric Nanogenerator by Filling High Dielectric Nanoparticles into Sponge PDMS Film. *ACS Appl. Mater. Interfaces* **2016**, *8*, 736–744. [CrossRef] [PubMed]
30. Zhou, Y.; Deng, W.; Xu, J.; Chen, J. Engineering Materials at the Nanoscale for Triboelectric Nanogenerators. *Cell Rep. Phys. Sci.* **2020**, *1*, 100142. [CrossRef]
31. Patsidis, A.C. Barium titanate/polydimethylsiloxane nano/ microcomposites fabrication, morphology, dielectric response and functionality. *IET Nanodielectrics* **2020**, *3*, 14–19. [CrossRef]
32. Jang, S.; Oh, J.H. Rapid Fabrication of Microporous $BaTiO_3$/PDMS Nanocomposites for Triboelectric Nanogenerators through One-step Microwave Irradiation. *Sci. Rep.* **2018**, *8*, 14287. [CrossRef]
33. Tantraviwat, D.; Ngamyingyoud, M.; Sripumkhai, W.; Pattamang, P.; Rujijanagul, G.; Inceesungvorn, B. Tuning the Dielectric Constant and Surface Engineering of a $BaTiO_3$/Porous PDMS Composite Film for Enhanced Triboelectric Nanogenerator Output Performance. *ACS Omega* **2021**, *6*, 29765–29773. [CrossRef] [PubMed]
34. Kim, Y.J.; Lee, J.; Park, S.; Park, C.; Park, C.; Choi, H.J. Effect of the relative permittivity of oxides on the performance of triboelectric nanogenerators. *RSC Adv.* **2017**, *7*, 49368–49373. [CrossRef]
35. Kim, J.; Ryu, H.; Lee, J.H.; Khan, U.; Kwak, S.S.; Yoon, H.J.; Kim, S.W. High Permittivity $CaCu_3Ti_4O_{12}$ Particle-Induced Internal Polarization Amplification for High Performance Triboelectric Nanogenerators. *Adv. Energy Mater.* **2020**, *10*, 1903524. [CrossRef]
36. Lee, J.W.; Ye, B.U.; Baik, J.M. Research Update: Recent progress in the development of effective dielectrics for high-output triboelectric nanogenerator. *APL Mater.* **2017**, *5*, 073802. [CrossRef]
37. Chen, J.; Wang, J.; Xuan, W.; Dong, S.; Luo, J. Universal triboelectric nanogenerator simulation based on dynamic finite element method model. *Sensors* **2020**, *20*, 4838. [CrossRef] [PubMed]
38. Hasan, S.; Kouzani, A.Z.; Adams, S.; Long, J.; Mahmud, M.A. Comparative study on the contact-separation mode triboelectric nanogenerator. *J. Electrost.* **2022**, *116*, 103685. [CrossRef]
39. Wang, Z.; Liu, W.; Hu, J.; He, W.; Yang, H.; Ling, C.; Xi, Y.; Wang, X.; Liu, A.; Hu, C. Two voltages in contact-separation triboelectric nanogenerator: From asymmetry to symmetry for maximum output. *Nano Energy* **2020**, *69*, 104452. [CrossRef]
40. Rodrigues, C.; Pires, A.; Gonçalves, I.; Silva, D.; OIiveira, J.; Pereira, A.; Ventura, J. Hybridizing Triboelectric and Thermomagnetic Effects: A Novel Low-Grade Thermal Energy Harvesting Technology. *Adv. Funct. Mater.* **2022**, *32*, 2110288. [CrossRef]
41. Zhou, Q.; Takita, R.; Ikuno, T. Improving the Performance of a Triboelectric Nanogenerator by Using an Asymmetric TiO_2/PDMS Composite Layer. *Nanomaterials* **2023**, *13*, 832. [CrossRef]